ISBN: 978-3-95450-257-8 ISSN: 2222-5692 doi:10.18429/JACoW-ECRIS2024-TUB2

SIMULATION OF SURFACE X-RAY EMISSION FROM THE ASTERICS ECR ION SOURCE

T. Thuillier*, B. Cheymol, A. Cernuschi, M. Kusulja, E. Lagorio, C. Peaucelle, F. Vezzu
Université Grenoble Alpes, CNRS-LPSC, INP Grenoble, Grenoble, France
M. Dubois, F. Lemagnen, Université Normandie, GANIL, Caen, France
T. Cadoux, H. Felice, D. Simon, Université Paris-Saclay, CEA-Irfu, Saclay, France

Abstract

The bremsstrahlung x-ray emission induced by the impact of plasma electrons deconfined on the chamber wall of the ASTERICS ion source is investigated by a suite of two simulations. First, the electron velocity and density distribution of lost electrons is calculated by a dedicated Monte-Carlo code. The specificity of the electron velocity, energy and spatial distribution function on the walls is presented and discussed. Second, the electron information is used as an input for the Fluka Monte-Carlo code, used to investigate the surface induced bremsstrahlung x-ray emission. The electron distribution temperature at the wall is found to be anisotropic and increases with $B_{\min}$. The electrons impinge the walls with large angles values with respect to the local normal surface, which has consequences on the emission direction of the x-ray. The x-ray dose is mapped inside and around the ion source for two cases: (i) for a low $B_{\min}$ magnetic confinement and an electron temperature set to 50 keV; and (ii) for a large $B_{\min}$ and an electron temperature artificially increased to 120 keV. The latter configuration gives a dose in the cave at 5 m from the source of ∼100 µSv/h per kW of impacting electrons. A set of internal tungsten shielding placed inside the source have been modelled to investigate the dose attenuation inside the cave. This shielding is very effective and significantly reduces the need for external x-ray shielding to spatially limited solid angles located on the injection side of the ion source, facilitating the source maintenance and associated safety processes.

ASTERICS ION SOURCE

The ASTERICS ion source is currently under development as part of the new GANIL injector (NEWGAIN) project [1], aiming at designing and building a second injector for the SPIRAL2 linear accelerator, able to manage heavy ion beams up to a mass over charge ratio equal to 7. ASTERICS is a 28 GHz ECR ion source using a superconducting magnet system, composed of a cos 3θ hexapole coil and 3 axial solenoids to generate the minimum-B confinement magnetic field [2, 3]. A cutaway view of the (work in progress) ion source design is proposed in Fig. 1. The superconducting magnet system is very close to the VENUS-FRIB design, except for the plasma chamber dimension which is enlarged to 600 mm length and 91 mm radius, in order to enhance the achievable ion beam intensities during operation. The goal is to produce steadily 10 pµA beams of U^{34+} for nuclear physics experiments lasting several weeks.

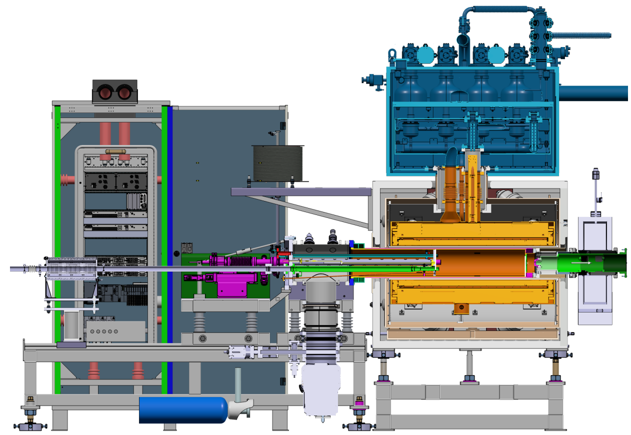

Figure 1: Cutaway view of the ASTERICS ion source design.

ELECTRON LOSSES TO THE WALL

An existing Monte-Carlo code was adapted to study the electron dynamics inside the ASTERICS ion source plasma chamber [4]. The 28 GHz radio-frequency (RF) electric field considered in the simulation is modelled with a transverse travelling plane wave with a circular polarization and a constant electric field intensity E = 10 kV/m (corresponding to 7 kW of injected RF power). Electrons are randomly generated inside the ECR volume with a random velocity direction in space. The initial electron energies are randomly sampled using a set of Gaussian distributions centered on each argon ionization potential energies IP with a standard deviation of 10 % × IP, with a relative abundance following a typical argon ion spectrum having a mean charge state number of 8. The electrons are tracked until they touch the 3 possible walls: injection at $z_{\text{inj}} \approx -0.3$ m, extraction at $z_{\text{ext}} \approx 0.3$ m and radial wall at $r_W = 0.091$ m. Two static electric fields are modelled in the Monte-Carlo simulation. One for the injection biased disk with a voltage of 100 V and a diameter of 20 mm. The second for the accelerating electric field of the ion source on the extraction, being 10 kV/cm, extending for 4 cm right after the extraction electrode hole of 10 mm diameter. The electrons are propagated up to 1 ms and are stopped above this time limit. Coulomb collision and electron impact are considered in the simulation to model at best the electron deconfinement. The plasma density considered is 15 % of the cut-off density at 28 GHz. A set of 1.25×10^6 electrons was simulated for each magnetic configuration.

* thomas.thuillier@lpsc.in2p3.fr

ISBN: 978-3-95450-257-8 ISSN: 2222-5692 doi:10.18429/JACoW-ECRIS2024-TUB2

The electron final positions and velocities on the plasma chamber wall were stored and analysed.

The electron particle distribution at the plasma chamber wall was studied for two axial magnetic field configurations: 3.7-0.3-2.2 T and 3.7-0.8-2.2 T, deemed representative of the actual ion source operation. The hexapolar radial magnetic field intensity at wall is fixed at 2.4 T. The $B_{\min}$ = 0.3 T configuration, suitable for double frequency operation (18+28 GHz), is known to generate a low output flux of energetic x-rays [5]. On the contrary, the $B_{\min}$ = 0.8 T configuration experimentally maximises the production of high energy x-rays [5–7]. The aforementioned magnetic configurations are used to probe the minimum and maximum x-ray dose in the accelerator cave, respectively. The electron energy distribution function (EEDF) of the electrons impacting the walls are plotted in Fig. 2(a) and Fig. 2(b) for the magnetic configurations $B_{\min}$ = 0.3 and 0.8 T respectively. The EEDF for the injection, radial and extraction walls are reported in each subplot in black, blue and red respectively. The high energy part of individual EEDF have been fitted with a Maxwell-Boltzmann distribution, and the temperature obtained with the fit are reported in the Table 1 for each surface and magnetic configuration. It is interesting to note that the EEDF both varies on the wall surface location and with the intensity of $B_{\min}$. The normalized counts per wall surface associated with $B_{\min}$ = 0.3 and 0.8 T are proposed in Table 2. One can note a transfer of the flux of electrons from the radial (76 to 52 %) to the extraction wall (17 to 41 %) when $B_{\min}$ is changed from 0.3 to 0.8 T.

Table 1: Estimation of the EEDF high energy tail temperature obtained on the injection, radial and extraction plasma chamber walls for $B_{\min}$ = 0.3 and 0.8 T.

Axial profile	$\mathbf{T_{inj}}$	$\mathbf{T_{rad}}$	$\mathbf{T_{ext}}$
3.7-0.3-2.2 T	19.8 ± 1.6	41.7 ± 1.5	44.0 ± 7.4
3.7-0.8-2.2 T	36.0 ± 8.6	52.0 ± 3.1	63.2 ± 7.9

Table 2: Distribution of the final position of the electrons for the two magnetic axial profiles considered. The subscripts $\%_{inj}$, $\%_{ext}$ and $\%_{rad}$ refer respectively to the particles deconfined at the injection, extraction and radial walls. $\%_{conf}$ stands for the amount of electrons still confined at the time limit of 1 ms.

Axial profile	$\mathbf{\%_{inj}}$	$\mathbf{\%_{ext}}$	$\mathbf{\%_{rad}}$	$\mathbf{\%_{conf}}$
3.7-0.3-2.2 T	3.2	17.3	76.0	3.6
3.7-0.8-2.2 T	5.8	41.5	52.1	0.6

The reason for this shift is a change of the minimum magnetic field intensity at the plasma chamber wall, which passes from 2.03 to 2.29 T, making the weakest magnetic point the extraction peak field (2.2 T) for the latter case (see [8] for details). The increase of $B_{\min}$ is coming along with a temperature increase of the hot electrons ($T_{\rm rad}$ from 41 to 52 keV, $T_{\rm ext}$ from 44 to 63 keV). This specific topic is thoroughly discussed in another paper dedicated to the ASTERICS plasma x-ray volume emission [8]. It is also worth noting that, for $B_{\min}$ = 0.8 T, the 3 EEDF feature a visible hump for E ≈ 15-20 keV, which is known to cause plasma instabilities and has been confirmed experimentally for such a high $B_{\min}$ [9]. Figure 3 presents the distribution of angle of incidence θ of electrons hitting the plasma chamber wall ($\theta = \widehat{(\vec{v}, \vec{n})}$, $\vec{n}$ local normal to the surface) for (a) $B_{\min}$ = 0.3 and 0.8 T. The color plot convention in Fig. 3 is identical to the one adopted in Fig. 2. One can observe how the magnetic field intensity strongly influences the distribution shape. While the distributions for the injection are almost identical for (a) and (b), one can observe a stronger peaking of the extraction wall distribution when $B_{\min}$ is increased from 0.3 to 0.8 T,

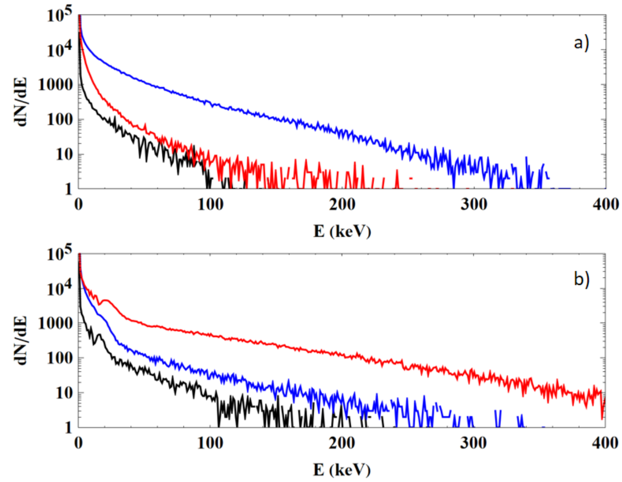

Figure 2: EEDF of the electrons hitting the plasma chamber wall for **(a)** $B_{\min}$ = 0.3 T and **(b)** $B_{\min}$ = 0.8 T. The black, blue and red plots are respectively recorded on the injection ($z=z_{\rm inj}$), radial ($r=r_{\rm wall}$) and extraction surfaces ($z=z_{\rm ext}$).

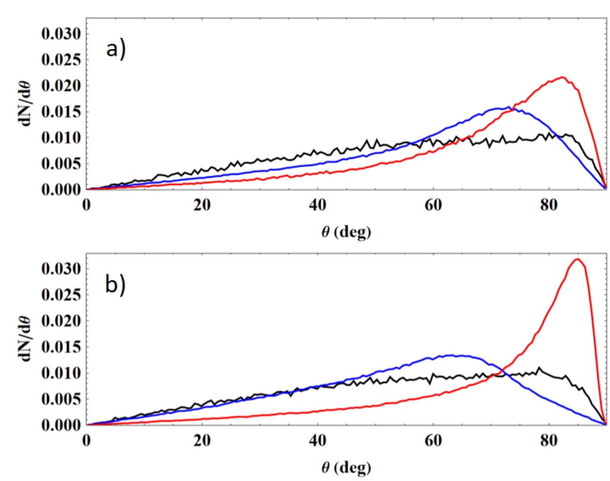

Figure 3: Distribution of the angle of incidence of electron impacting the plasma chamber walls ($\theta = \widehat{(\vec{v}, \vec{n})}$), $\vec{n}$ normal to the surface) **(a)** for $B_{\min}$ = 0.3 T and **(b)** for $B_{\min}$ = 0.8 T. The black, blue and red curves correspond to the injection, radial and extraction surfaces respectively.

ISBN: 978-3-95450-257-8 ISSN: 2222-5692 doi:10.18429/JACoW-ECRIS2024-TUB2

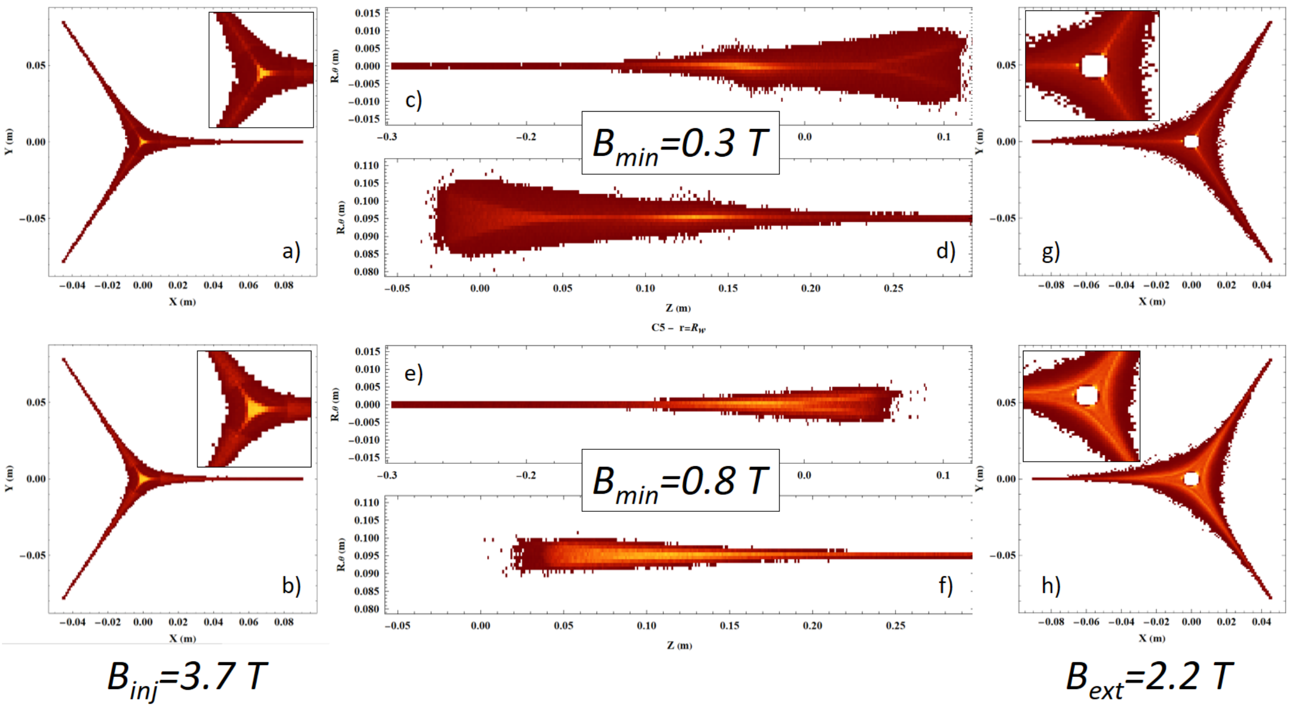

Figure 4: Electron density distribution at the injection ((a) and (b)), radial ((c), (d), (e) and (f)) and extraction ((g) and (h)) surface of the plasma chamber wall for B_{min} = 0.3 T (top plots) and B_{min} = 0.8 T (bottom plots). The dimension scale of images between the top and the bottom is conserved.

with a most probable angle of ≈ 85°. And on the other hand, a concomitant reduction of the most probable impact angle at the radial wall is found, from 72° to 65°. The high values of θ are a consequence of the magnetic mirror effect, which converts the electron parallel velocity (to the local magnetic field vector) into transverse velocity. The direction of impact of electrons on the wall influences the direction of emission of bremsstrahlung photons and must be considered in the bremsstrahlung simulation. The electron distribution of electrons on the injection, radial and extraction wall is proposed for B_{min} = 0.3 and 0.8 T in Fig. 4. While the injection electron distribution is marginally affected on the injection surface (with a triangular core centered on the axis which is twice larger when B_{min} = 0.8 T), one can observe how the distribution is significantly re-balanced between the radial and the extraction walls. At B_{min} = 0.8 T, the radial electron distribution is concentrated on a much smaller surface, while the place where high flux of electron hit the extraction wall is largely enhanced, showing by the way a distribution shape that is usually observed in ECRIS when they are dismounted.

X-RAY FLUX SIMULATION

A simplified version of the ASTERICS source's geometry, its extraction system and the first meter of its low energy beam transfer line have been modelled with Fluka [10], as can be seen in Fig. 5. The output of the MC electron simulation (position and velocity direction) was used as an input for the Fluka code. The electron energy was independently cast assuming a Maxwell-Boltzmann distribution with temperatures of 50 keV for B_{min} = 0.3 T and 120 keV for B_{min} = 0.8 T respectively. The boost of the electron temperature with respect to the one given by the MC simulation is necessary to enhance the rate of primary high energy electrons, required to produce energetic bremsstrahlung photons able to exit the source and contribute to the external dose in a reasonable simulation time. The 50 keV temperature is selected to represent a typical example of operation which minimizes the x-ray dose emitted from the source, while the 120 keV value presents an over-estimation by 20 % of the highest temperature expected during the safe and stable ion source operation [5–7]. The latter configuration is used to dimension the x-ray shielding of the ASTERICS source. In Fluka, the secondary particles showers (mainly photons and electrons) generated by each primary electron are followed until they are fully stopped by matter. The local electron position and velocity distribution of each of the three plasma chamber surface (injection, radial and extraction walls) is used to start an independent Fluka simulation.

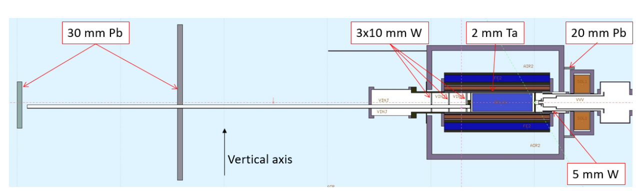

Figure 5: Sectional view of the ion source geometry modelled with Fluka. Detail of the materials geometry used to shield the x-ray emission from the source are provided. See text for details.

26th Int. Workshop Electron Cyclotron Resonance Ion Sources ECRIS2024, Darmstadt, Germany JACoW Publishing
ISBN: 978-3-95450-257-8 ISSN: 2222-5692 doi:10.18429/JACoW-ECRIS2024-TUB2

The 3 simulations results are next merged to obtain the full x-ray spectrum of the ion source. Preliminary investigations have shown that a non-negligible amount of initial electrons impinging the walls bounce back toward the plasma chamber, especially when θ is getting close to 90°. A bouncing electron would follow a magnetic field line and hit the chamber wall elsewhere, following the initial distribution condition rules provided as input to Fluka. It is deemed unnecessary to track further such electrons (which is highly time-consuming in Fluka), since it is approximately equivalent to cast a fresh electron instead. The riddance of these parasitic electrons is achieved by defining a volume area inside the source composed of gas with a hard rule to stop any electron below 3 MeV, while the gas remain quasi-transparent to secondary x-ray photons crossing it.

Figure 6 presents the x-ray fluence per electron generated impinging (a) the injection surface, (b) the radial wall and (c) the extraction surface when B_{min}/kT_e = 0.8 T/120 keV. One can see that the dominant x-ray photon leak able to exit the source occurs on the source injection side, at the place where the material thickness is the lowest. The whole photon flux incoming towards the superconductor cold mass is stopped in the first radial centimeters. The 5 cm thick iron yoke surrounding the superconducting magnet cryostat also strongly attenuates the x-ray flux passing through it. On the other hand, the x-rays exiting on the extraction side are either directed along the beam pipe axis or channelled radially in the gap between the source and the first focusing solenoid yoke.

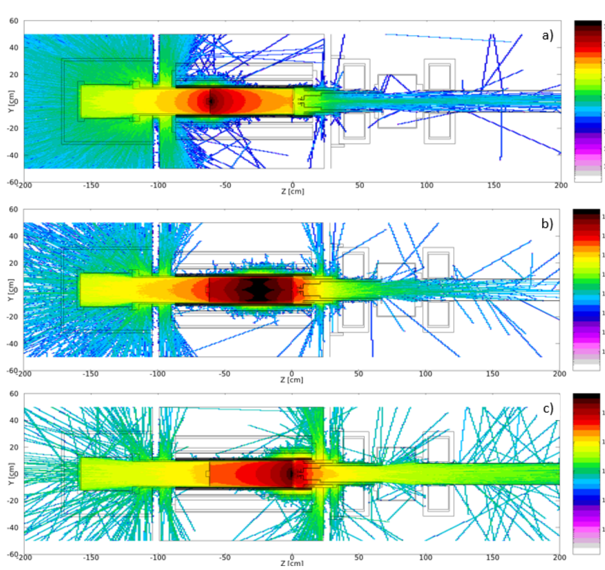

Figure 6: Averaged x-ray fluence generated by the impact of a single electron on injection (a), radial (b), and extraction walls (c) when B_{min} = 0.8 T and kT_e = 120 keV.

Table 3 presents the total x-ray yield per electron generated for B_{min}/kT_e = 0.3 T/50 keV and 0.8 T/120 keV. It is striking to note that the configuration 0.8 T/120 keV favours the leak of photons toward the injection and extraction walls (27 and 62 % respectively) rather than the radial direction (11 % only). This counterintuitive effect is likely a consequence of the following facts: (i) an increase of the electron yield on the extraction wall for B_{min} = 0.8 T (see Table 2), (ii) a high rate of electrons bouncing the walls and (iii) x-ray traversing thick material layers are subject to diffusion and back-scattering, favoring the remaining photons to escape toward the direction with the lesser matter (injection and extraction). On the other hand, one should remember that Fluka propagates all the secondary particles generated by the incident electron until the particle shower ends. The yields presented in Table 3 also include numerous lower energy photons subject to high scattering probability, which would finally not be detected outside the ion source.

Table 3: Total x-ray photon to electron yield passing through the injection, radial and extraction wall surfaces, for B_{min} = 0.3 and 0.8 T.

Axial profile	photon / e^-	%Inj	%rad	%ext
3.7-0.3-2.2 T	5.7×10^{-5}	15 %	60 %	25 %
3.7-0.8-2.2 T	1.6×10^{-4}	27 %	11 %	62 %

The ion source cave was added to the simulation to study the dose around the source without extra x-ray shielding. The result is displayed in Fig. 7(a). One can see that the local dose can be as high as ~100 µSv per kW of injected electrons in the corridor located on the left (Z<−600 cm) along the ion source axis, on its injection side. Because a maximum dose rate of 7.5 µSv is allowed in this corridor, a local shielding of the source was studied with Fluka. The shielding presented here includes a set of three 10 mm thick tungsten screens, located under vacuum inside the ion source core, installed behind the plasma injection flange, as can be seen in Fig. 5.

The shields modelled are hollowed by a set of three 40 mm diameter holes, mimicking the passage of two metallic ovens and the 28 GHz oversized waveguide. Since the latter is pointing axially toward the plasma, the copper wave guide was also modelled to study the x-ray dose distribution. The x-ray escaping the three holes are next stopped by a 30 mm thick lead shield located in the cave at the end of the injection system frame and set to ground potential. This shield dimension is limited to a small solid angle and is located far away from the place where the daily maintenance of the source is done. A second local 30 mm lead shield (not represented) was added at the waveguide bend to stop any x-ray channeled in the waveguide. Finally, a 5 mm thick lead shield is fixed along the fences closing the ion source high voltage zone. On the extraction side, the x-rays are blocked by a 5 mm thick cylinder around the extraction system and by a 20 mm thick cylinder closing the radial gap between the source yoke and the extraction solenoid yoke. The resulting x-ray dose after filtering is displayed in Fig. 7(b), showing only places where the dose is higher than 5 µSv/h per kW of electrons. One can check that the modelled compact shielding screens efficiently prevent the x-ray dose to extend outside the cave. The dose in the corridor on the left is lower than 1 µSv/h.

ISBN: 978-3-95450-257-8 ISSN: 2222-5692 doi:10.18429/JACoW-ECRIS2024-TUB2

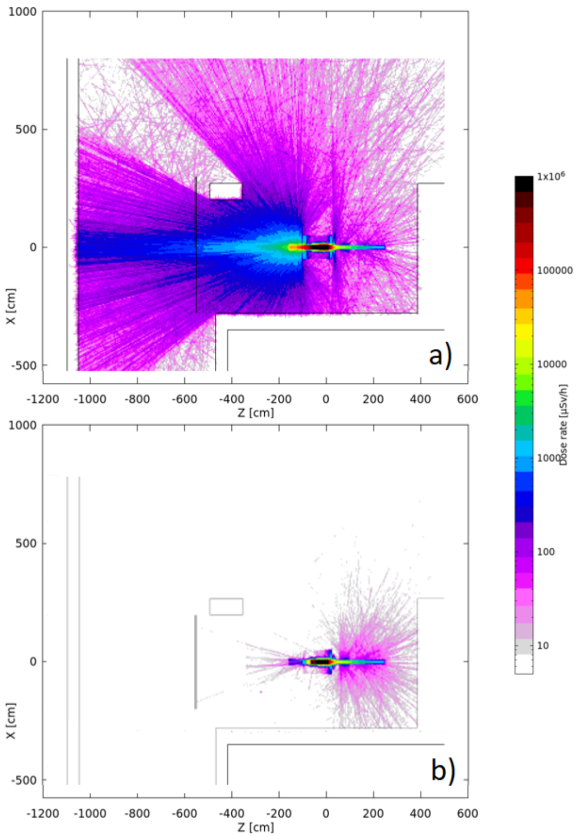

Figure 7: X-ray dose per kW of electron simulated in the cave (a) without and (b) with shielding when $B_{\min} = 0.8\,\mathrm{T}$ and $kT_e = 120\,\mathrm{keV}$.

CONCLUSION

The x-ray dose exiting the ASTERICS ion source has been studied with Fluka, using as input the results of a MC electron code simulating the hot electron dynamics in the ECRIS. The MC code results indicate a strong spatial electron temperature anisotropy at the three plasma chamber walls: injection, radial and extraction. An increase of the electron temperature at the three walls is obtained when $B_{\min}$ increases. The distribution of electron flux to these surfaces is also found to be strongly dependent on the value of $B_{\min}$: electron flux leaks preferentially toward the place where the magnetic field of the Minimum-B structure is minimum. This behaviour is a consequence of the electron Coulomb scattering in the plasma. The distributions of angle of incidence of the electrons with respect to the normal to the local surface present a peak above 60° and 80° for the radial and extraction walls respectively. These distribution angles are a consequence of the magnetic mirroring effect happening in the strongly magnetized ECRIS. The large angle of incidence of electron to the wall results in a large amount of them being bounced back toward the plasma. It also results in specific solid angles of photon emissions that must be considered to appropriately simulate the x-ray spatial emission distribution from ECRIS. Without shielding, a dose higher than ~100 μSv/h per kW of electrons is obtained in the corridor located at a distance of 5 m from the injection side of the ECRIS in the NEWGAIN cave. A preliminary shielding composed of several plates of tungsten placed inside the source, under vacuum and as close as possible to the plasma chamber, are used to attenuate the x-ray dose in the cave. Such a solution allows reducing dramatically the places where x-ray shielding must be placed around the ECRIS, which results in a simplified ion source maintenance and a simpler and cheaper radiation safety design.

ACKNOWLEDGEMENT

This work is supported by Agence Nationale de la Recherche, with the contract # 21-ESRE-0018 EQUIPEX+ NEWGAIN.

REFERENCES

[1] M. Moscatello *et al.*, "NEWGAIN project at GANIL-SPIRAL2: design of the new heavy ion injector for the superconducting LINAC", in *Proc. 14th Int. Part. Accel. Conf. (IPAC'23)*, Venice, Italy, pp. 1747–1749, 2023. doi:10.18429/JACoW-IPAC2023-TUPA193

[2] D. Simon *et al.*, "Design of ASTERICS: A superconducting 28 GHz ECR ion source magnet for GANIL", *IEEE Trans. Appl. Supercond.*, vol. 33, no. 5, p. 4 002 905, 2023. doi:10.1109/TASC.2023.3260779

[3] T. Thuillier *et al.*, "ASTERICS, a new 28 GHz electron cyclotron resonance ion source for the SPIRAL2 accelerator", *J. Phys. Conf. Ser.*, vol. 2743, no. 1, p. 012 059, 2024. doi:10.1088/1742-6596/2743/1/012059

[4] T. Thuillier *et al.*, "Investigation on the electron flux to the wall in the VENUS ion source", *Rev. Sci. Instrum.*, vol. 87, no. 2, p. 02A736, 2015. doi:10.1063/1.4935989

[5] J. Benitez, C. Lyneis, L. Phair, D. Todd, and D. Xie, "Dependence of the Bremsstrahlung Spectral Temperature in Minimum-B Electron Cyclotron Resonance Ion Sources", *IEEE Trans. Plasma Sci.*, vol. 45, no. 7, pp. 1746–1754, 2017. doi:10.1109/TPS.2017.2706718

[6] D. Neben *et al.*, "X-ray investigation on the Superconducting Source for Ions (SuSI)", *J. Instrum.*, vol. 14, no. 02, p. C02008, 2019. doi:10.1088/1748-0221/14/02/C02008

[7] J. B. Li *et al.*, "Effects of magnetic configuration on hot electrons in a minimum-b ecr plasma", *Plasma Phys. Controlled Fusion*, vol. 62, no. 9, p. 095 015, 2020. doi:10.1088/1361-6587/ab9d8f

[8] A. Cernuschi and T. Thuillier, "Effect of magnetic configuration on hot electrons in a minimum-B ECR plasma", *To be submitted to Phys. Rev. Accel. Beams*.

[9] O. Tarvainen *et al.*, "Limitations of electron cyclotron resonance ion source performances set by kinetic plasma instabilities", *Rev. Sci. Instrum.*, vol. 86, no. 2, p. 023 301, 2015. doi:10.1063/1.4906804

[10] G. Battistoni *et al.*, "Overview of the fluka code", *Ann. Nucl. Energy*, vol. 82, pp. 10–18, 2015. doi:10.1016/j.anucene.2014.11.007